PHYSICAL REVIEW D **75,** 064005 (2007)

Head-on collisions of boson stars

C. Palenzuela,[1] I. Olabarrieta,[1,2] L. Lehner,[1] and S. L. Liebling[3]

[1]*Department of Physics and Astronomy, Louisiana State University, 202 Nicholson Hall, Baton Rouge, Louisiana 70803-4001, USA*
[2]*TELECOM Unit, ROBOTIKER-Tecnalia, Edificio 202 Parque Tecnológico Zamudio E-48170, Bizkaia, Spain*
[3]*Department of Physics, Long Island University–C.W. Post Campus, Brookville, New York 11548, USA*
(Received 13 December 2006; published 2 March 2007)

We study head-on collisions of boson stars in three dimensions. We consider evolutions of two boson stars which may differ in their phase or have opposite frequencies but are otherwise identical. Our studies show that these phase differences result in different late time behavior and gravitational wave output.

DOI: 10.1103/PhysRevD.75.064005 PACS numbers: 04.25.Dm

I. INTRODUCTION

Models of compact ''stars'' described by nonfluid sources serve both as probes of strong-field gravity and as exotic alternatives to the standard ''regular'' fluid stars. Among these nonstandard star models, a geon—a self-gravitating star consisting of electromagnetic fields—was first considered by Wheeler [1]. Despite its appeal, no stable geon could be constructed and so interest diminished. However, borrowing from this idea, Kaup was able to construct the first stable configuration—referred to as a *Klein-Gordon geon*—by considering a U(1) classical scalar field [2]. Soon after Kaup's construction, Ruffini and Bonazzola revisited the solution, adopting a quantum point of view while the geometry was maintained as a classical entity [3]. By employing a Hartree-Fock (multiparticle) approximation, they reobtained Kaup's equations (and hence solutions), providing an alternative view to the resulting stars. These solutions are currently known as *boson stars* and describe a family of self-gravitating scalar-field configurations within general relativity.

Boson stars have been studied in many different contexts (see [4,5] for reviews). They have been proposed as models for dark matter (see [6] for a recent review) and more recently have been used as convenient models for compact objects including black holes [7]. One can consider strongly gravitating compact-star spacetimes without the worries associated with regular matter—such as shock fronts and discontinuities in the fluid variables—making boson stars very useful probes of strong-field general relativity.

Given this utility, a number of efforts have modeled the dynamical evolution of boson stars. For instance, they have been considered in one and two dimensions for studies of critical phenomena [8,9]. In three dimensions, studies of the dynamics of perturbed boson stars have been presented in [10,11] and preliminary collisions in [12]. Works examining boson-star collisions in two dimensions were carried out in [8] while in three dimensions, in addition to our own, another effort is under way [13]. Another work which studies the collisions of Q-balls also has relevance here [14]. These Q-balls are solitonic solutions of the Klein-Gordon (KG) equations in the absence of gravity with an attractive potential.

In this paper we investigate several boson-star configurations paying particular attention to head-on collisions in 3D. Our aim is to survey some of the phenomenology that can be found in these scenarios. Additionally, since one can employ this particular physical system to describe strongly gravitating compact stars, one can use them to model compact systems in general relativity in their early stages where tidal effects are not too severe. On a more speculative level, one can also examine the gravitational wave signature produced so that searches by gravitational wave detectors might place constraints on their existence.

The paper is organized as follows. In Sec. II we detail the formalism we use for the Einstein-Klein-Gordon (EKG) system. Section III describes the numerical implementation of the governing equations. In Sec. IV we present our results. We conclude in Sec. V, adding some final comments. The computation of the initial data for a single boson star is described in Appendix A, while Appendix B is devoted to some (qualitative) physical considerations in order to explain the results of the simulations.

II. THE EINSTEIN-KLEIN-GORDON SYSTEM

The dynamics of a complex scalar field in a curved spacetime is described by the following Lagrangian density (adopting geometrical units, i.e. $G = c = 1$) [15],

$$\mathcal{L} = -\frac{1}{16\pi}R + \frac{1}{2}[g^{ab}\partial_a\bar{\phi}\partial_b\phi + V(|\phi|^2)]. \quad (1)$$

Here R is the Ricci scalar, g_{ab} is the spacetime metric, ϕ is the scalar field, $\bar{\phi}$ its complex conjugate, and $V(|\phi|^2)$ a potential depending only on $|\phi|^2$. Throughout this paper roman letters at the beginning of the alphabet, $a, b, c, \ldots$, denote spacetime indices ranging from 0 to 3, while letters near the middle, $i, j, k, \ldots$, range from 1 to 3, denoting spatial indices. This Lagrangian gives rise to the equations determining the evolution of the metric (Einstein equations) and those governing the scalar-field behavior (Klein-Gordon equations).

A. Einstein equations

The variation of the action associated with the Lagrangian (1) with respect to the metric g_{ab} leads to the Einstein equations

$$R_{ab} - \frac{R}{2} g_{ab} = 8\pi T_{ab}, \tag{2}$$

where R_{ab} is the Ricci tensor and T_{ab} is the stress-energy tensor given by

$$T_{ab} = \tfrac{1}{2}[\partial_a \bar{\phi} \partial_b \phi + \partial_a \phi \partial_b \bar{\phi}] - \tfrac{1}{2} g_{ab}[g^{cd} \partial_c \bar{\phi} \partial_d \phi + V(|\phi|^2)]. \tag{3}$$

The Einstein equations form a system of 10 nonlinear partial differential equations for the spacetime metric components g_{ab}. A convenient way to express the equations can be obtained by the identity

$$R_{ab} = -\tfrac{1}{2} g^{cd} \partial_c \partial_d g_{ab} + \partial_{(a} \Gamma_{b)} - \Gamma_{cab} \Gamma^c + g^{cd} g^{ef} (\partial_e g_{ca} \partial_f g_{db} - \Gamma_{ace} \Gamma_{bdf}), \tag{4}$$

where we have introduced the quantities

$$\Gamma_a \equiv g^{bc} \Gamma_{abc}, \tag{5}$$

$$\Gamma_{abc} = \tfrac{1}{2}(\partial_b g_{ac} + \partial_c g_{ab} - \partial_a g_{bc}). \tag{6}$$

Up to this point we have considered arbitrary coordinates x^a that label spacetime points. In order to define an initial value problem for the Einstein equations, a foliation defined by the hypersurfaces with $x^0 \equiv t = \text{const}$ is introduced with the (normalized) vector $n_a = -\nabla_a t / ||\nabla_a t||$, where ∇_a is the covariant derivative associated with g_{ab}. The harmonic formulation of Einstein equations exploits the fact that the coordinates x^a can be chosen satisfying the harmonic $\nabla^c \nabla_c x^a = 0$ [16] or their generalized version [17,18]

$$\nabla^c \nabla_c x^a = -\Gamma_a = H^a(t, x^i), \tag{7}$$

where the functions H^a amount to prescribing coordinate conditions. These expressions can be combined to reexpress Einstein equations (2) in their generalized harmonic form, as [17,19]

$$g^{cd} \partial_{cd} g_{ab} + \partial_a H_b + \partial_b H_a = -16\pi \left(T_{ab} - \frac{T}{2} g_{ab} \right) + 2\Gamma_{cab} H^c + 2 g^{cd} g^{ef} [\partial_e g_{ac} \partial_f g_{bd} - \Gamma_{ace} \Gamma_{bdf}]. \tag{8}$$

Notice that the partial derivatives of H^a do not belong to the principal part of the system since they are prescribed spacetime functions. The principal part of (8) is a well-posed system of decoupled wave equations for the 10 metric components. It is important to stress that Eqs. (8) with the generalized harmonic condition (7) constitute an overdetermined system since Γ_a can be obtained either from the choice of coordinates (7) or from the evolution of the metric itself (8). In the free-evolution approach, Eq. (8) is adopted to update the metric, and Eq. (7) is regarded as a constraint on the full system. Possible constraint violations can be measured by introducing a new four-vector [20],

$$2Z^a \equiv -\Gamma^a - H^a(t, x^i). \tag{9}$$

Clearly, the physical solutions will be those satisfying the algebraic condition $Z_a = 0$ throughout the spacetime; we will refer to the Z_a quantities as the Z-constraints from now on. Note that added flexibility, useful for numerical purposes, is attained by adding these constraints to the equations. In particular, since the addition of these Z-constraints to the evolution system can change the stability of the solutions against perturbations off the constraint surface, one can exploit this fact to one's advantage. Indeed, suitable terms can be added to the equations in order to construct an attractor for the physical solutions in certain spacetimes, in such a way that small Z-constraint violations will be damped during the evolution [21]. With these damping terms, Eq. (8) can be written as

$$g^{cd} \partial_{cd} g_{ab} + \partial_a H_b + \partial_b H_a = +2\Gamma_{cab} H^c + 2 g^{cd} g^{ef} [\partial_e g_{ac} \partial_f g_{bd} - \Gamma_{ace} \Gamma_{bdf}] - 2\sigma_0 [n_a Z_b + n_b Z_a - g_{ab} n^c Z_c] - 16\pi \left(T_{ab} - \frac{T}{2} g_{ab} \right) \tag{10}$$

where we have introduced σ_0, which is a free parameter that controls the damping of the Z-constraints (9).

B. Klein-Gordon equations

As mentioned, the variation of the Lagrangian (1) with respect to the scalar field ϕ leads to the KG equations

$$\Box \phi = \frac{dV}{d|\phi|^2} \phi, \tag{11}$$

where the box $\Box = g^{ab} \nabla_a \nabla_b$ stands here for the wave operator on a curved background. For concreteness, from now on we will consider the free field case where the potential takes the form

$$V(|\phi|^2) = m^2 |\phi|^2, \tag{12}$$

with m a parameter that can be identified with the bare mass of the field theory times $\hbar$ [2]. With the convention adopted here ($\hbar = 1$), m has inverse length units. For

simplicity, we have fixed its value to unity. The potential (12) leads to the so-called *miniboson stars*, because achievable stable configurations have small masses. More general terms can be included, such as the $\lambda|\phi|^4$ self-interaction term introduced in [22], leading to heavier *boson stars* which have masses and sizes more relevant to astrophysical applications when considering their compactification ratio. In the present work we restrict ourselves to the $\lambda = 0$ case, deferring to a future work the study of the effect of this self-interacting term.

C. Reduction of the complete system to first order

The second order EKG equations (10) and (11) can be employed to obtain the future evolution of the spacetime if $\{g_{ab}, \phi, g_{ab,t}, \phi_{,t}\}$ are provided at an initial hypersurface. For a numerical implementation, it is also useful to further reduce the system to fully first order to take advantage of several numerical techniques devised to exploit stability theorems for these kinds of systems [23–26]. Consequently, these techniques provide a clean path to discretize the system in a robust manner [27–29]. Thus we begin by reducing these equations to first order form.

The reduction in time is achieved by introducing new independent variables related to the time derivatives of the fields. Following a similar route as in [19], we define

$$Q_{ab} \equiv -n^c \partial_c g_{ab}, \qquad \Pi \equiv -n^c \partial_c \phi. \tag{13}$$

The evolution equations for Q_{ab} and Π are now given by the EKG equations (10) and (11), while the evolution equations for g_{ab} and ϕ are simply given by their definition (13).

The reduction to first order in space is made by introducing new independent variables, encoding the first space derivatives as

$$D_{iab} \equiv \partial_i g_{ab}, \qquad \Phi_i \equiv \partial_i \phi. \tag{14}$$

The equations of motion for these quantities are obtained by applying the time derivative to their definition (14) and imposing that time and spatial derivatives commute. Notice that in this step, just as with the Z-constraints, one encounters an overdetermined system since spatial derivatives can be obtained either by deriving the fields or from the evolution equation of the new quantities (14). This fact can be reinterpreted as adding new constraints to the system,

$$\mathcal{C}_{iab} = \partial_i g_{ab} - D_{iab} = 0, \qquad \mathcal{C}_i = \partial_i \phi - \Phi_i = 0, \tag{15}$$

which must be satisfied for a consistent solution. An analogous situation is encountered with the conditions

$$\begin{aligned} \mathcal{C}_{ijab} &= \partial_i D_{jab} - \partial_j D_{iab} = 0, \\ \mathcal{C}_{ij} &= \partial_i \Phi_j - \partial_j \Phi_i = 0 \end{aligned} \tag{16}$$

resulting from the commutativity of the second spatial derivatives. Henceforth we will refer to the $\{\mathcal{C}_i, \mathcal{C}_{ij}, \mathcal{C}_{iab}, \mathcal{C}_{ijab}\}$ quantities as the C-constraints. At this point the resulting first order system is described by the evolution equations for the array of fields $\{g_{ab}, Q_{ab}, D_{iab}, \phi, \Pi, \Phi_i\}$ together with the Z-constraints (9) and C-constraints (15) and (16).

Additionally, as with the Z-constraints, the mathematical properties of the evolution system can be changed—when the constraints are not exactly satisfied—by judiciously adding the C-constraints to the right-hand side of the equations. For instance, in [19] these constraints are incorporated in the equations in such a way that the physical solutions (i.e., those satisfying $\mathcal{C}_i = \mathcal{C}_{ij} = \mathcal{C}_{iab} = \mathcal{C}_{ijab} = 0$) are an attractor in certain spacetimes. This means that small C-constraint violations will also be damped during the evolution. We follow the same approach here for the full first order reduction of the Einstein Klein-Gordon equations by writing them as

$$\partial_t g_{ab} = \beta^k D_{kab} - \alpha Q_{ab}, \tag{17}$$

$$\begin{aligned} \partial_t Q_{ab} = {} & \beta^k \partial_k Q_{ab} - \alpha \gamma^{ij} \partial_i D_{jab} - \sigma_1 \beta^k \partial_k g_{ab} - \alpha \partial_a H_b \\ & - \alpha \partial_b H_a + 2\alpha \Gamma_{cab} H^c \\ & + 2\alpha g^{cd} (\gamma^{ij} D_{ica} D_{jdb} - Q_{ca} Q_{db} - g^{ef} \Gamma_{ace} \Gamma_{bdf}) \\ & - \frac{\alpha}{2} n^c n^d Q_{cd} Q_{ab} - \alpha \gamma^{ij} D_{iab} Q_{jc} n^c + \sigma_1 \beta^k D_{kab} \\ & - 16\pi\alpha \left(T_{ab} - \frac{g_{ab}}{2} T \right) \\ & - 2\alpha\sigma_0 [n_a Z_b + n_b Z_a - g_{ab} n^c Z_c], \end{aligned} \tag{18}$$

$$\begin{aligned} \partial_t D_{iab} = {} & \beta^k \partial_k D_{iab} - \alpha \partial_i Q_{ab} + \alpha \sigma_1 \partial_i g_{ab} \\ & + \frac{\alpha}{2} n^c n^d D_{icd} Q_{ab} + \alpha \gamma^{jk} n^c D_{ijc} D_{kab} \\ & - \alpha \sigma_1 D_{iab}, \end{aligned} \tag{19}$$

$$\partial_t \phi = \beta^k \Phi_k - \alpha \Pi, \tag{20}$$

$$\begin{aligned} \partial_t \Pi = {} & \beta^k \partial_k \Pi - \alpha \gamma^{ij} \partial_i \Phi_j - \sigma_1 \beta^k \partial_k \phi - \frac{\alpha}{2} \Pi n^c n^d Q_{cd} \\ & - \alpha \gamma^{ij} \Phi_i n^c Q_{jc} + \alpha \Gamma_c \Phi^c + \alpha m^2 \phi + \sigma_1 \beta^k \Phi_k, \end{aligned} \tag{21}$$

$$\begin{aligned} \partial_t \Phi_i = {} & \beta^k \partial_k \Phi_i - \alpha \partial_i \Pi + \alpha \sigma_1 \partial_i \phi + \frac{\alpha}{2} \Pi n^c n^d D_{icd} \\ & + \alpha \gamma^{jk} \Phi_k n^c D_{ijc} - \alpha \sigma_1 \Phi_i \end{aligned} \tag{22}$$

where σ_1 is another free parameter that controls the damping of the first order constraints (15) and (16). Additionally, we have introduced the familiar lapse α and shift β^i functions for convenience. These are defined through the relations $\beta^i = \gamma^{ij} \beta_j$ (γ_{ij} being the spatial projection of g_{ab} satisfying $\gamma^{il} \gamma_{lj} = \delta^i_j$, $g_{ti} = \beta_i$) and $g^{tt} = \alpha^{-2}$.

Equations (17)–(22) constitute the final set of equations being integrated in our implementation.

D. Analysis quantities

One way to identify the position of the boson star, which might be difficult in the fully dynamical case, is to use the energy density $\rho \equiv n^a n^b T_{ab}$. We have used the maximum of ρ, at each temporal slice, to represent the center of each starlike configuration.

Another useful quantity, which is of special interest in the case of the boson-antiboson collision, is the Noether charge of the theory. Because of the U(1) symmetry of the stress-energy tensor, there is a conserved quantity which can be computed by

$$N = \int J^0 dx^3, \qquad J^0 = \frac{i}{2}\sqrt{-g}g^{0\nu}[\bar{\phi}\partial_\nu\phi - \phi\partial_\nu\bar{\phi}]. \tag{23}$$

We employ the Noether density J^0 to give additional evidence as to the location of the boson star. As discussed in [3], this quantity can be associated with the number of bosonic particles.

The mass of the stars is computed by means of the ADM mass, which is defined as

$$M = \frac{1}{16\pi}\lim_{r\to\infty}\int g^{ij}[\partial_j g_{ik} - \partial_k g_{ij}]\mathcal{N}^k dS \tag{24}$$

where $\mathcal{N}^k$ stands here for the unit outward normal to the sphere.

The gravitational radiation is described asymptotically—when the correct tetrad and coordinates are adopted—by the Newman-Penrose (spin-weighted) Ψ_4 scalar. This quantity is defined as

$$\Psi_4 = C_{abcd}\mathrm{n}^a\bar{\mathrm{m}}^b\mathrm{n}^c\bar{\mathrm{m}}^d, \tag{25}$$

with C_{abcd} being the Weyl tensor and where n^a denotes the incoming null normal to the extraction worldtube Γ while $\bar{\mathrm{m}}^a$ is the complex conjugate of the null vector tangent to Γ at a constant time slice. (Note that the tetrad vector n^a is not to be confused with the unit normal to the hypersurface n^a.)

To analyze the structure of the radiated waveforms it is convenient to decompose the signal in -2 spin-weighted spherical harmonics as

$$r\Psi_4 = \sum_{l,m} C_{l,m}\,{}^{-2}Y_{l,m} \tag{26}$$

where the factor r is included to better capture the $1/r$ leading order behavior of Ψ_4. For head-on collisions of nonspinning objects, one could take advantage of the natural axis of symmetry defined by the line joining the centers of the objects. In such a case, the (spin-weighted) spherical harmonics ${}^sY_{l,m}$ can be defined such that the radiation produced in the axisymmetric configuration would display essentially only $m = 0$ modes. However, as we are interested in more general cases also, we adopt spherical harmonics defined with respect to an axis that can be regarded as orthogonal with respect to the orbital plane, which in our present case is given by the z axis. In this case, the radiation extracted would have nontrivial components for $m \neq 0$.

We also focus on integral quantities that are independent of the specific basis of the spherical harmonics, such as the radiated energy. In terms of Ψ_4, we can write

$$\frac{dE}{dt} = \frac{r_{\mathrm{ext}}^2}{4\pi}\int_\Omega\left[\left|\int_{-\infty}^{t}\Psi_4(t')dt'\right|\left|\int_{-\infty}^{t}\bar{\Psi}_4(t')dt'\right|\right]d\Omega, \tag{27}$$

where $\bar{\Psi}_4$ denotes the complex conjugate of Ψ_4, and r_{ext} is the extraction radius. Using both the decomposition (26) and the orthonormalization of the spherical harmonics, this expression can also be written as

$$\frac{dE}{dt} = \frac{1}{4\pi}\sum_{l,m}|D_{l,m}|^2, \qquad D_{l,m} = \int_{-\infty}^{t} C_{l,m}(t')dt'. \tag{28}$$

Finally, we will assume that the resulting coordinates in the neighborhood of the extraction surfaces satisfy, to a reasonable level, conditions ensuring Ψ_4 is essentially free of spurious effects (aside from those arising from the extraction at finite distances) [30,31]. Detailed studies of the possible influences of these in more general settings will be presented elsewhere [32].

III. IMPLEMENTATION ISSUES

The first order symmetric hyperbolic system (17)–(22) is implemented following techniques devised to take advantage of several useful theorems which guarantee the stable implementation of linear hyperbolic systems. In general, these techniques involve (i) discrete derivative operators satisfying summation by parts (SBP), which allow defining a semidiscrete norm and an energy estimate for the solution [24,26], (ii) a method of lines employing a third order Runge-Kutta operator for the time integration that preserves the energy estimate in the fully discrete case [25], and (iii) maximally dissipative boundary conditions that keep this energy bounded in time [23] in the presence of boundaries. The combination of techniques (i)–(iii) guarantee that linear problems are implemented stably and thus provides a direct route to a robust implementation of generic first order hyperbolic systems. Additionally, we introduce a Kreiss-Oliger type dissipative operator (suitably modified at/near boundary points so as not to spoil the energy estimate [27,28]). The introduction of dissipation allows one to control the high frequency modes of the solution which are always poorly described by a finite difference approach. In what follows we provide further details of the particular application of these techniques in the present work.

A. Discrete operators and time evolution

We have adopted second order derivative operators satisfying SBP and defined a discrete energy essentially as the L_2 norm of the solution, that is,

$$E = \sum_A ||U_A|| \equiv \sum_A \sum_{I,J,K} U_A(I,J,K)^2 \tag{29}$$

where $U_A = \{g_{ab}, Q_{ab}, D_{iab}, \phi, \Pi, \Phi_i\}$ is an array with all the evolved variables and $U_A(I,J,K)$ is the value of U_A at the grid point (I,J,K). The energy estimate is obtained when the discrete operators reduce to the standard three-point centered derivative operator at interior points with the standard (first order) two-point sideways stencil at boundary points. The particular form for the Kreiss-Oliger fourth order dissipation operator is described in [27,28] as is the third order Runge-Kutta scheme employed to advance the solution in time.

We additionally employ the norm of the Z-constraints,

$$||Z|| = \sum_{a=0}^{3} ||Z_a||, \tag{30}$$

to monitor the deviation of the numerical solution from the physical one.

B. Characteristic structure

As mentioned, we employ maximally dissipative boundary conditions. These conditions rely on knowing the characteristic mode structure of the principal part of the system. In essence, these conditions bound the amount of "energy" the incoming modes introduce at the boundaries to remain below what the outgoing modes carry away from the computational domain. Schematically, this reduces to adopting conditions satisfying $w^- = L w^+$ with w^-, w^+ denoting incoming/outgoing modes at a given boundary, and L a bounded matrix [24]. As a result, the norm (29) of the solution remains bounded in the linear regime, which is key to ensure the well posedness of the initial boundary value problem (for details see [23–25]). In our particular case, we choose $L = 0$, thus setting the incoming modes to zero. The characteristic decomposition (eigenmodes w with velocity v) for the EKG system (17)–(22) is given by

$$\begin{aligned} {w_{ab}}^0 &\equiv g_{ab}, & v^0 &= 0, \\ {w_{iab}}^\beta &\equiv D_{iab} - \mathcal{N}^k D_{kab} \mathcal{N}_i, & v^\beta &= -\mathcal{N}_k \beta^k, \\ {w_{ab}}^{(\pm)} &\equiv Q_{ab} - \sigma_1 g_{ab} \pm \mathcal{N}^k D_{kab}, & & \\ & & v^\pm &= -\mathcal{N}_k \beta^k \pm \alpha \end{aligned} \tag{31}$$

with $\mathcal{N}^k$ the outgoing normal vector to the boundary surface; the supra-indices $\{0, \beta, \pm\}$ denote modes propagating with the different speeds $\{v^0, v^\beta, v^\pm\}$. Thus the incoming modes are given by w^-_{ab} and ${w_{iab}}^\beta$ as long as $\mathcal{N}_k \beta^k < 0$. To apply the maximally dissipative conditions at the numerical level, we follow the prescription described in [23,27] and simply enforce

$$\partial_t {w_{ab}}^{(-)} = 0, \tag{32}$$

$$\partial_t w^\beta_{iab} = 0, \quad \text{if } \mathcal{N}_k \beta^k < 0. \tag{33}$$

We point out that these boundary conditions, although key for ensuring stability, are not enforcing the constraints. Thus, constraint violations are expected to arise (and propagate inwards) at the boundaries. Constraint preserving boundary conditions [19] are being implemented in the code and will be employed in future projects.

C. Mesh refinement

Adaptive mesh refinement (AMR) provides increased resolution where and when needed, and therefore becomes an essential tool in resolving a wide range of dynamical scales, both spatial and temporal. As described by Berger and Oliger [33], a given numerical grid can be further refined based on dynamical measures of the numerical error by the creation of refined grids which are evolved in sync with the coarse grid. We have built our code taking advantage of the computational infrastructure called HAD (an outgrowth of the code presented in [34,35]). HAD implements a (slight) modification of the standard Berger-Oliger strategy that guarantees preserving the stability properties of the unigrid implementation and significantly reduces spurious reflections at interface boundaries [36]. In HAD creation or destruction of finer grids is automated so that points which display an error above some threshold are "covered" by a finer grid. The error associated with each point is computed via a self-shadow hierarchy [37]. In this technique, the error is computed on any given grid by subtracting the solution on that grid with that on the next coarser level. Because these solutions evolve with different resolutions, their difference represents a measure of the local truncation error without recourse to more complicated shadow schemes. In particular, at any given point, the L_2 norm of the difference between the solutions over all evolved fields is taken as the truncation error estimate. Although we have performed binary boson-star runs employing AMR, in this work we take only partial advantage of the mesh refinement capabilities of HAD. One reason for this is that we want to compare significantly different scenarios and we find it useful to ensure that similar discretizations are employed across the cases considered. Our procedure is to let the infrastructure define the grid structures at the initial time and keep it fixed throughout the simulations. The truncation error value employed by the self-shadow hierarchy to define the grids is chosen such that the original stars are contained within the finest grid and that this grid covers the whole region in between. Fixing the grid structure at the initial time reduces some of the overhead and memory required by dynamic regridding.

IV. SIMULATIONS AND RESULTS

In this section we describe the simulations we have performed both to check the correctness of the implementation and investigate interesting aspects of boson-star head-on collisions. We begin in Sec. IV A, by considering a single isolated boson-star configuration and verify that the code is able to reproduce known features of the solution. The evolution of the star is performed employing two different coordinate systems, the static one and the harmonic one. The former coordinate system is the natural one employed in constructing a single static boson-star solution, and so the evolution with it should be trivial. The latter one does not conform to the ansatz employed to obtain the solution and some nontrivial gauge dynamics can be expected.

In Sec. IV B we consider different binary systems described by boson stars with zero initial momentum. Initial data for these systems are obtained by a simple superposition of a single boson star with another which is identical to it up to a possible phase or reflection of its natural frequency. The stars are placed sufficiently far from each other to ensure the constraints are satisfied to a degree consistent with the value obtained in the single boson-star case.

We have performed three different types of head-on collisions: collisions of equal boson stars (Sec. IV B 1), collisions of boson stars whose phases are in opposition (Sec. IV B 2), and finally collisions of boson stars with antiboson stars (Sec. IV B 3) (these differences are explained in detail below).

For all of the simulations presented here we have adopted damping parameters $\sigma_0 = \sigma_1 = 1$, a Courant factor $\Delta t/\Delta x = 0.25$, and Kreiss-Oliger dissipation parametrized by 0.03 (as described in [27,28]). The simulations have been performed on 64 to 128 processors employing three refinement levels, placed as defined by the shadow hierarchy.

A. The single boson star

As described in the Introduction, a boson star is a self-gravitating configuration of the scalar field with the Lagrangian given by (1). In a particular coordinate system, one assumes a particular form for the spherically symmetric scalar field

$$\phi = \phi_0(r)e^{-i\omega t}. \tag{34}$$

Therefore the field values at any given point oscillate with a constant frequency ω. Details of the calculation of $\phi_0(r)$ are presented in Appendix A. The geometry, on the other hand, remains static in these same coordinates. This solution provides a reasonable model for a compact object in equilibrium.

We have carried out simulations of single boson stars under two coordinate choices. The initial data for the coordinate evolution are the same in both cases, but the equations determining their evolution differ. These equations are obtained by either exploiting the requirement of staticity or by adopting harmonic conditions. In Sec. IV A 1 we summarize the results in the coordinate system on which the solution is static, and the results in the harmonic gauge are presented in Sec. IV A 2. The simulations presented for both cases employ a grid structure consisting of three levels of refinement. The finest level covers the radius R_{95} of the star (defined as region of space containing approximately 95% of the star's mass) while the resolution decreases a factor 2 on the box surrounding it. For all these runs the star is located at $x^i = 0$ $(i = 1 \ldots 3)$ and the computational domain is given by $x^i \in [-144, 144]$.

To obtain a measure of the convergence rate of the solution, we have performed simulations with different resolutions for the boxes. The finest grid of each resolution considered has $\Delta x \in \{0.375, 0.25, 0.156\}$ for the static coordinates and $\Delta x \in \{0.5, 0.375, 0.25\}$ for the harmonic ones. The others grids, as mentioned, have a gradual 2:1 ratio in their discretization length.

Below we detail certain convergence tests of the code about which we would like to make a general comment. Residuals of constraints are expected to approach zero with increases in resolution while field variables should approach a unique solution, and this behavior is indeed what we find. The rate of convergence can also be examined and compared to the expected approximation order of the difference equations solved, and we found the expected second order convergence in the unigrid case. However, when dealing with a complicated grid hierarchy, precise measurements of this rate become somewhat problematic, especially when the hierarchies produced vary with the truncation error threshold chosen. Also, we should mention that more detailed convergence tests with this code infrastructure applied to other problems demonstrate the expected order of convergence [36,38].

1. Single boson star in static coordinates

In order to maintain the coordinates such that the spacetime remains static, the $H^a(t, x^i)$ functions in (7) need to be chosen in a suitable way. Since we are considering a static situation, the condition on H^a can be read directly from Eq. (9) by imposing the constraints (i.e., $Z^a = 0$) and the staticity of the spacetime (i.e., $\partial_t g_{ab} = 0$). In an explicitly static scenario, this initial value of the $H^a(t = 0, x^i)$ is preserved for all times.

We begin with initial data describing a star with the value of the scalar field at the origin being $|\phi_0(r = 0)| = 0.01$. This star, which is obtained by solving the initial-data problem with a high resolution one-dimensional code as described in Appendix A, has an ADM mass of $M_{1D} = 0.361$ and radius $R_{95} = 19.6$, and lies well inside the stable branch of solutions.

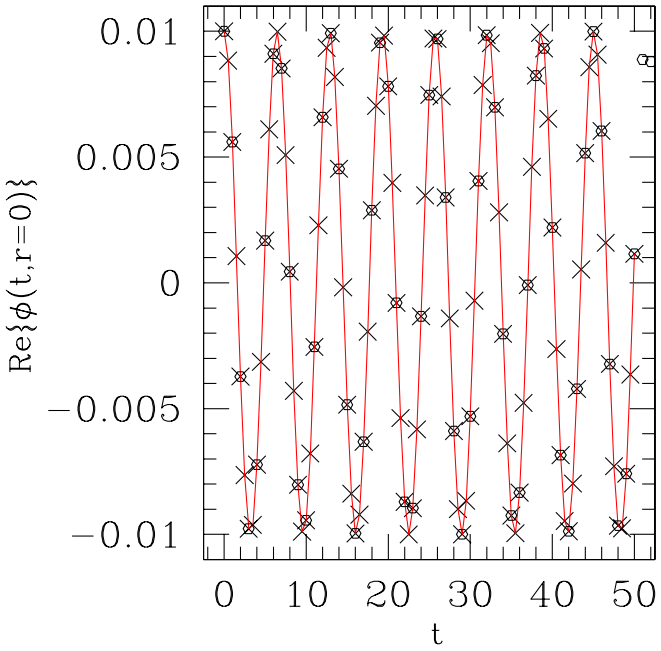

FIG. 1 (color online). *Single boson star.* Phase oscillation of the real part of the scalar field at the center of symmetry up to $t = 50$ for the resolution $\Delta x = 0.25$ (similar behavior was followed up to $t = 500$). The solid line indicates the analytically expected value, the crosses show the values read off from the numerical solution within the static coordinates, and the circles show the same by using the harmonic coordinates.

The evolution of an isolated star displays the expected behavior. In particular, the evolution of the scalar field agrees with Eq. (34) as demonstrated in Fig. 1 where the central value of the real part of the scalar field versus time describes an oscillatory behavior with a frequency $\omega = 0.96 \pm 0.03$. This result is in excellent agreement with the frequency obtained with the one-dimensional initial-data problem code $\omega_{1D} = 0.976$. Also, the geometry is static, as can be seen in Fig. 2 with the evolution of the maximum of g_{xx} as a function of coordinate time t for three different resolutions.

2. Single boson star in harmonic coordinates

In this section we revisit the initial data of the previous one, but in this case we do not adopt coordinate conditions that explicitly demonstrate the staticity of the spacetime. One goal of this exercise is to test the ability of the harmonic-coordinate condition to adapt to the physical problem under consideration. This will be important for the binary cases considered later, as that problem is certainly not static.

The implementation evolves the system for as long as the code was run without any signs of instabilities. For this particular case we have evolved the system for more than $t = 1500$. During this evolution, we have monitored the ADM mass which we extract at $r_{\rm ext} = 100$ and obtain $M = 0.364$ which decreases by less than 3%/1% for the coarsest/finest resolution considered ($\Delta x = 0.5/0.25$ for the innermost grid) by the time we stop the code. This illustrates the ability of the code to preserve this conserved quantity for long times.

We have also checked that, for this particular solution, both the harmonic and the static coordinates agree at the center of symmetry. This implies that the scalar field should have the same local oscillatory behavior (34) at $r = 0$ in both coordinate systems. This is indeed the case and is illustrated in Fig. 1. In particular, the measured oscillation frequency is $\omega = 0.97 \pm 0.06$, Additionally, we have checked that the absolute value of the scalar field at the center of the star varies by at most 12%/2% for the coarsest/highest resolution considered.

Coordinate effects do arise however. As mentioned above, the geometry should have some nontrivial coordinate-induced dynamics since we are not adopting a coordinate system on which the solution is explicitly static. This effect can be seen in Fig. 3 where the evolution of the maximum of g_{xx} as a function of coordinate time t for three different resolutions is displayed. As evident in the figure, there is an initial transient variation of the metric value which later approaches a constant value.

Finally, we monitor the constraints in Fig. 4. The figure shows the L_2 norm (30) of the physical constraints [i.e., the

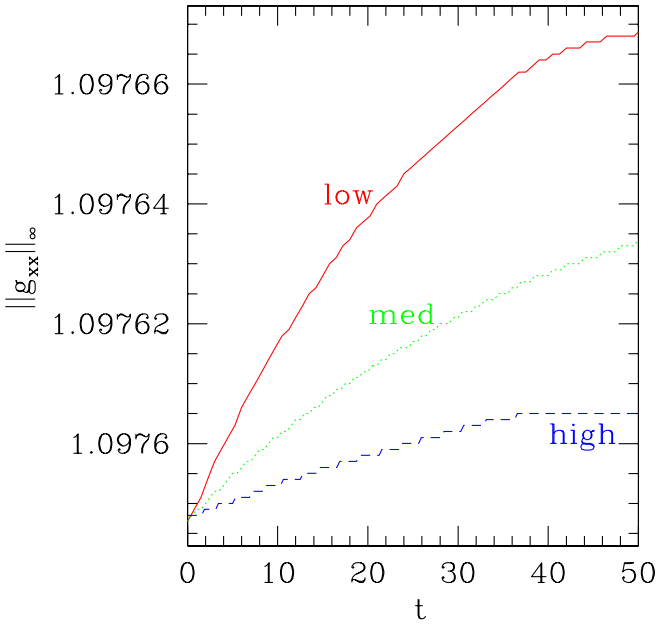

FIG. 2 (color online). *Single boson star.* L_∞ of g_{xx} versus time for the solution obtained employing the static coordinate condition. The figure displays the result of the evolution for three different base resolutions $\Delta x = \{0.375, 0.25, 0.156\}$ (in addition, each numerical solution is obtained with three levels of refinement). The values obtained converge to a constant value as expected, and the maximum variation observed to $t = 50$ is $\simeq 0.0073\%$ for the coarsest base resolution while for the highest one it is just $\simeq 0.0015\%$.

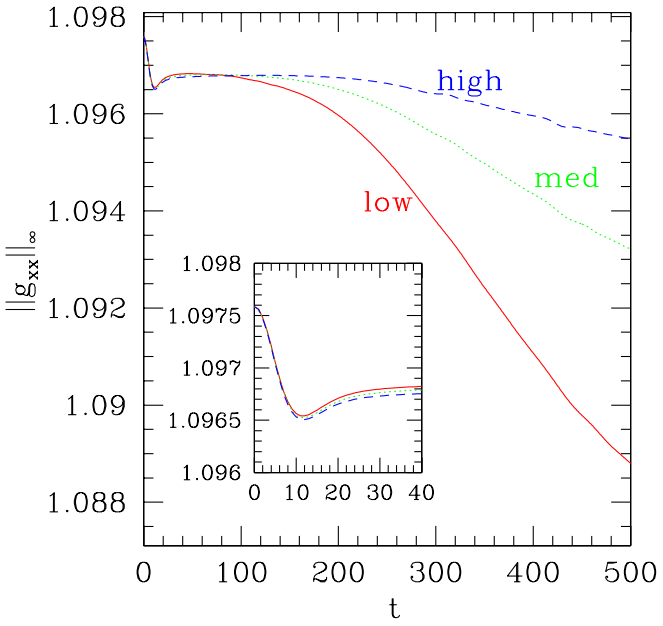

FIG. 3 (color online). *Single boson star.* L_∞ of g_{xx} versus time for the solution obtained employing the harmonic-coordinate condition. The figure displays the result of the evolution for three different base resolutions $\Delta x = \{0.25, 0.375, 0.50\}$ (in addition, each numerical solution is obtained with three levels of refinement). After a small transient behavior, the values obtained converge to a constant value. The maximum variation observed to $t = 500$ is $\simeq 0.72\%$ for the coarsest base resolution while $\simeq 0.11\%$ for the highest one.

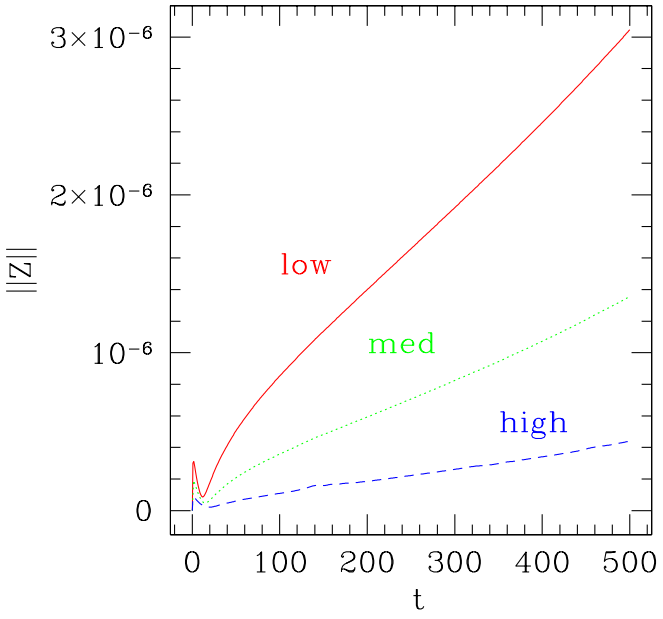

FIG. 4 (color online). *Single boson star.* Convergence of the L_2 norm of the Z-constraint residual [defined by Eq. (30)] versus time by using harmonic coordinates, for the same resolutions as in Fig. 3. As the resolution is increased the constraint violation is clearly reduced.

Z-constraints (9)] and its behavior when the resolution is improved, converging clearly to zero. The measured convergence rate is 2.9 between the low-and-medium and 2.8 between the medium-and-high resolutions.

B. Binary boson-star head-on collisions

Initial data for the collision of two boson stars is obtained by a simple superposition of the single boson solution in a way described below. Additionally, in order to consider different configurations, we take advantage of the following observations:

(i) The solution of the initial-data problem is unaffected by a phase difference in the ansatz assumed for the scalar field. Namely, $\phi = \phi_0(r)e^{i(wt+\theta)}$ gives rise to the same initial data for $\{g_{ab}, \partial_t g_{ab} = 0\}$.

(ii) If $\{g_{ab}, \phi_0, \partial_t g_{ab} = 0, \partial_t \phi = i\omega\phi_0\}$ provides consistent initial data, so does $\{g_{ab}, \phi_0, \partial_t g_{ab} = 0, \partial_t \phi = -i\omega\phi_0\}$. The difference is solely in a frequency reflection of the boson star and is known as an antiboson star.

We will exploit these observations to consider what we will refer to as a boson in phase opposition by taking $\theta = \pi$ in (i) and/or an antiboson in (ii).

The initial data we consider is schematically represented by considering the following construction:

$$\begin{aligned} \phi &= \phi^{(1)}(x - x_1, y, z) + \phi^{(2)}(x - x_2, y, z), \\ \psi &= \psi^{(1)}(x - x_1, y, z) + \psi^{(2)}(x - x_2, y, z) - 1, \\ \alpha &= \alpha^{(1)}(x - x_1, y, z) + \alpha^{(2)}(x - x_2, y, z) - 1 \end{aligned} \tag{35}$$

where $u^{(i)}$ denotes the corresponding field of the boson i, centered at $(x_i, 0, 0)$, and the value of $\phi^{(i)}$ will be dictated by the type of boson star considered, that is, a boson star, a boson star in phase opposition, or an antiboson star. Notice that three fields (the scalar field ϕ, the conformal factor ψ, and the lapse α) are enough to set initial data consistent with the EKG equations, as described in Appendix A. Under this approach we are making the assumption that the boson stars are described with a single global scalar field ϕ instead of considering two sets of complex scalar fields to represent each star. This choice fixes in a straightforward way the interaction of the stars.

In order to consistently choose the initial position of the boson stars, we have measured, at the initial time, the L_∞ norm of the Hamiltonian constraint for different coordinate separations of the centers D. Since at sufficiently large distances the adopted data satisfies the constraints by construction, the constraint's behavior versus D provides a measure of the distance that must be adopted. As illustrated in Fig. 5, the error decreases very rapidly with separation and we have chosen the value $D = 50$ (which corresponds to $x_1 = -x_2 = 25$) that is close to the asymptotic behavior. In addition, we will use for all the head-on collisions the same form of the scalar function $\phi_0(r)$ in order to compare easily the different cases.

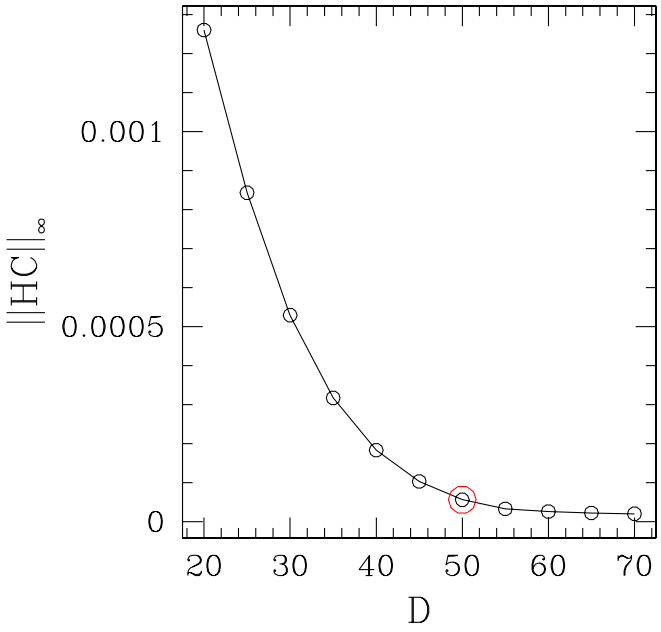

FIG. 5 (color online). *Boson/boson pair.* L_∞ norm of the Hamiltonian constraint residual versus the initial (coordinate) separation of the boson stars. As the distance is increased the violation decreases as expected since each star is defined so as to satisfy the constraints. We choose a value of $D = 50$ which lies close to the asymptotic behavior and is still manageable in terms of the boundaries.

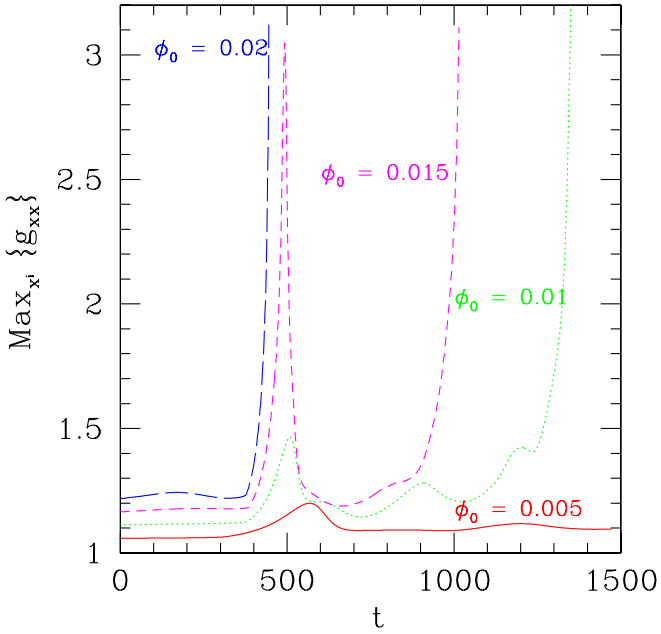

FIG. 6 (color online). *Boson/boson pair.* Geometry behavior for different central values of the scalar field that defines the stars. As the stars merge, the behavior of geometric variables changes drastically for different values. Stars with initial central densities >0.005 seem to give rise to a black hole as illustrated by their considerable growth; those below this value yield much smoother behavior. This is illustrated in the figure which displays the maximum of the component of the metric g_{xx} versus time for different central amplitudes of the scalar field $\{\phi_0 = 0.02, 0.015, 0.01, 0.05\}$, respectively. These give rise to stars with masses $\{M = 0.47, 0.42, 0.36, 0.26\}$, respectively.

1. Merging of the boson/boson pair

In this case, two identical boson-star configurations are adopted to define the initial data. Since the stars adopted have no initial velocity, their initial behavior is marked by a slow approach towards each other as they feel their gravitational attraction. As the evolution progresses, however, the resulting behavior depends on the mass of the single initial boson stars. Previous studies which concentrated on a particular set of initial masses always displayed a collision of stars giving rise to the formation of a black hole [12]. More recently, the work of [8,39], which considered boosted stars with large kinetic energy, presented cases where the stars appear to pass through each other in a sort of ''solitonic'' behavior.

Here we want to study the situation in which there is a final regular object (that is, containing no singularities). To do so we begin with a broad parameter search along the masses of the boson stars, searching for cases where the final compact object does not collapse to a black hole. As shown in Fig. 6, for stars with masses around $M = 0.26$ [corresponding to an amplitude of $\phi_0(r = 0) = 0.005$] the final object appears to avoid black hole formation. This avoidance is indicated by the geometric variables tending to a smooth, slow, oscillatory behavior for $M < 0.26$ while a marked violent behavior is displayed for larger values, together with a collapse of the lapse function.

We thus focus on the particular case where each star has masses $M = 0.26$, which is approximately 40% of the maximum allowed mass on the stable branch for the potential (12). The radius of the single star is around $R_{95} = 27$, and in this case we extend the computational domain to $x^i \in [-320, 320]$. As mentioned above, the refinement regions are rectangular boxes covering the centers of the stars and the span between them with a grid spacing at the region of the star of $\Delta x = 0.50$ for the lowest resolution and $\Delta x = 0.375$ for the highest one. We compute the values of the ADM mass and Ψ_4 at extraction surfaces located at $r_{\rm ext} = 140$, 170, and 200, where the grid spacing is given by $\Delta x = 4$ for the lowest resolution and $\Delta x = 3$ for the highest one (i.e., there are three levels of refinement). Since the wavelength of the observed radiation is of the order $\lambda \simeq 100$, the traveling wave is well represented by the grid structure at the extraction location.

In an effort to ensure fidelity to the continuum problem, we monitor constraint residuals and convergence of the metric variables for these evolutions. Notice however that, again, the grid structure for different resolutions differs and so our evolutions do not lend themselves to a traditional convergence study. However, we do see the expected behavior, in that the constraint residuals decrease in regions where the resolutions differ and the fields indicate convergence to a common value. This is illustrated in Fig. 7 where

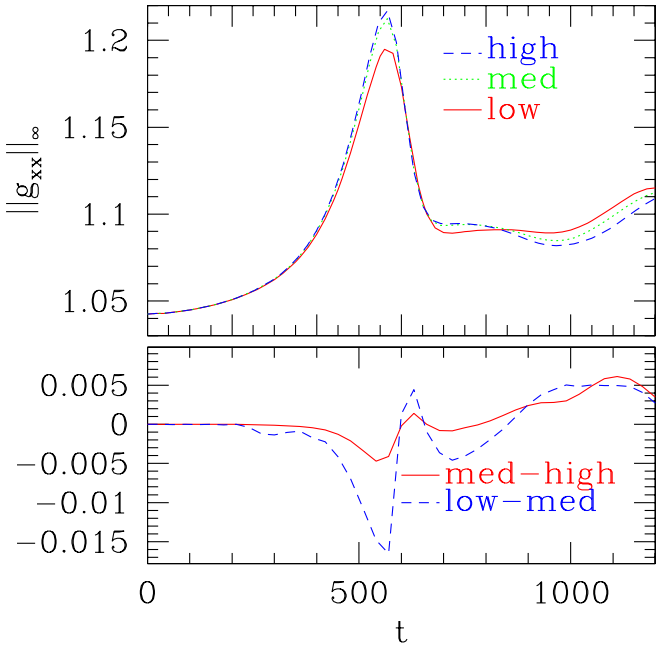

FIG. 7 (color online). *Boson/boson pair.* $L_\infty(g_{xx})$ as a function of time for three different resolutions and their differences. We can observe clearly that the merger occurs at approximately $t \simeq 550$. The solution is qualitatively convergent during the first part of the merger until $t \simeq 800$ when boundary effects negatively affect the convergence.

the maximum value of g_{xx} versus time is displayed. As evident in the plots, the values for different resolutions agree quite well until a time of about $t \simeq 800$ where accumulation of errors and boundary effects becomes apparent.

To illustrate the dynamics displayed by the solution, we present in Figs. 8 and 9 a sequence of plots illustrating the behavior of the Noether density J^0. The extremes of this function correspond, at least initially, to the centers of the stars and, as the evolution proceeds, the extremes give an indication as to the movement of the stars. Figure 8 presents two-dimensional slices (at $z = 0$) of J^0. Notice that the maximum value of J^0 is reached after the collision. This suggests that the boson stars have merged and oscillations of the merged object are clearly distinguishable. Figure 9 shows the nature of these oscillations in more detail by presenting contour plots of $J^0 = 2 \times 10^{-5}$ at more frequent times.

The gravitational radiation produced in the collision, as encoded in Ψ_4, is presented in Fig. 10 which illustrates the (real) coefficients of its $l = 2$ spin-weighted spherical harmonic modes. Because of the symmetry of this particular problem and with the spherical harmonics defined with respect to the z axis, there are the following simple relations between the nontrivial coefficients $C_{2,m}$,

$$\mathrm{Re}\{C_{2,2}\} = \mathrm{Re}\{C_{2,-2}\}, \qquad \mathrm{Re}\{C_{2,2}\} = -\sqrt{3/2}\,\mathrm{Re}\{C_{2,0}\}. \tag{36}$$

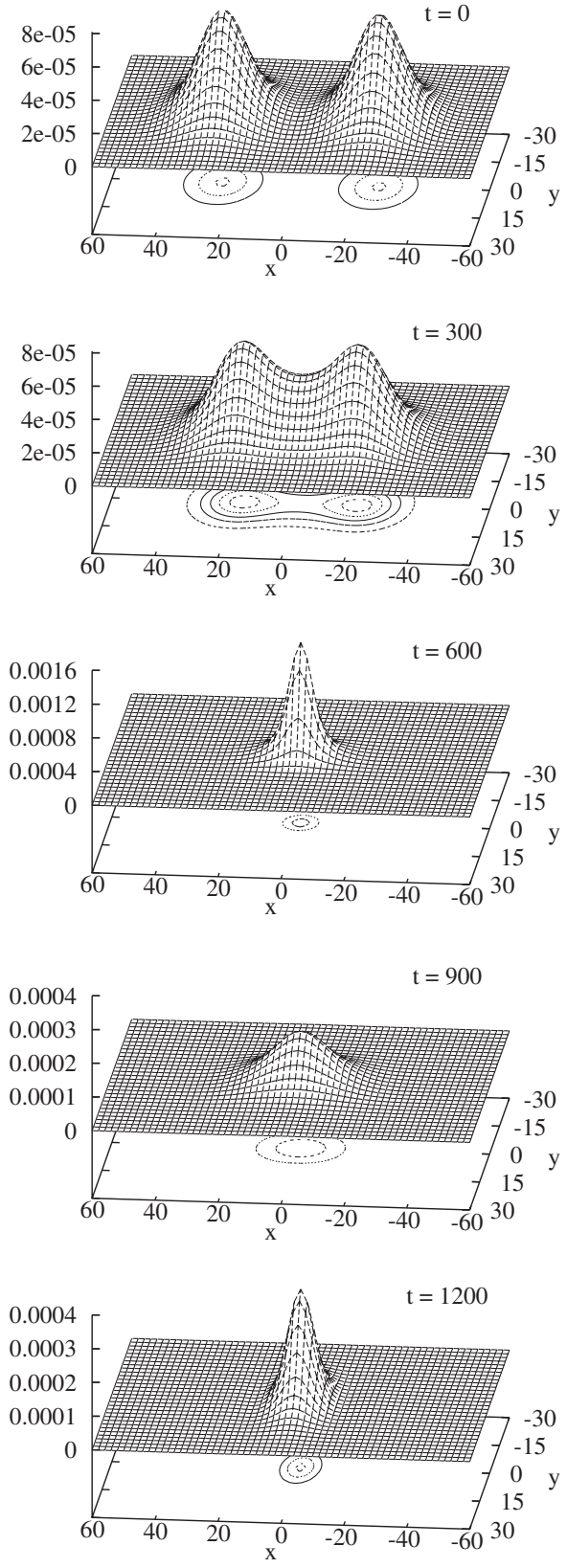

FIG. 8. *Boson/boson pair.* 2D $z = 0$ cuts of the Noether density J^0 at different times. As the stars come closer and merge, the maximum value of J^0 grows significantly, followed by a quadrupolar oscillation.

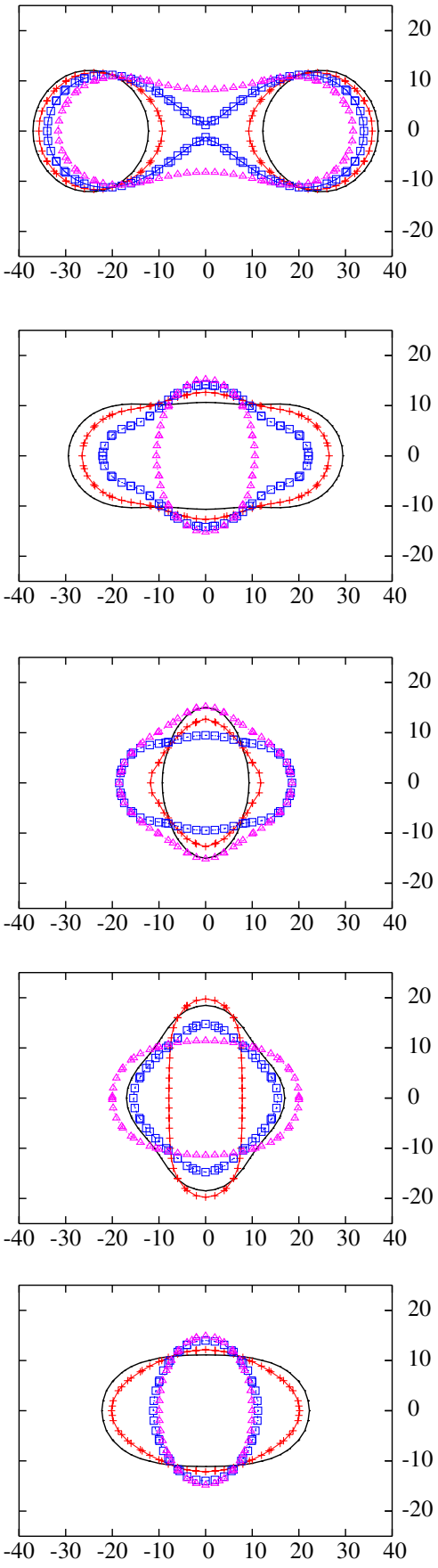

Numerically we have found that $\mathrm{Re}\{C_{2,2}\} = \mathrm{Re}\{C_{2,-2}\}$ and $\mathrm{Re}\{C_{2,2}\} = -1.22\ \mathrm{Re}\{C_{2,0}\}$, which is in excellent agreement with the expected analytical relations. The gravitational radiation emitted during the collision reaches the first extraction surface (at $r_{\mathrm{ext}} = 140$) at $t = 600$. It takes around $t = 200$–300 to reach the boundary, be reflected and pass again through the same extraction surface, as can be seen in Fig. 11. Notice that, despite having the surface extraction far from the sources, they are still not well within the "wave zone" since $r\Psi_4$ still displays a slight dependence on r_{ext}. Nevertheless, the structure of the radiated wave is evident in the plot.

In Fig. 12 we have plotted the emitted energy (or power) dE/dt [Eq. (28)] as a function of time for different resolutions. We find that practically all energy is radiated in the $l = 2$ mode which would simplify the parametrization of the obtained waveforms for their use in data analysis searches [31].

These evolutions therefore suggest that the merger of the two boson stars produces an oscillating single boson star. However, we note that the resulting star does not correspond to the boson star with mass equal to the sum of the individual masses. One might suspect the collision dispersed energy in the form of scalar and gravitational radiation, but that does not appear to be the case. The ADM mass hardly decreases and the gravitational wave output is minimal. Instead, it would appear that the resultant object has yet to settle into a stationary star.

2. Collision of boson/boson in opposition of phase pair

The case previously considered, in its early stages, can be regarded as generic for equal-mass objects in a head-on configuration. The inner-structure details only become relevant when the objects become sufficiently close to each other as indicated by the effacement theorem [40,41].

However, as the stars approach each other, the particular details of the star under consideration can have strong consequences. Let us consider the more general possibility of having a relative phase difference between the single boson stars that we will use to construct the global solution (35) as, for instance,

$$\phi^{(1)} = \phi_0(r)e^{-i\omega t}, \tag{37}$$

FIG. 9 (color online). *Boson/boson pair*. Contours corresponding to the value $J^0 = 2 \times 10^{-5}$ at the $z = 0$ plane. From top to bottom the contours are shown for times {0, 160, 240, 300}, {340, 380, 420, 460},{500, 540, 580, 640}, {680, 760, 840, 900}, and {980, 1060, 1140, 1200} indicated by solid lines, solid lines with crosses, solid lines with squares, and solid lines with triangles, respectively, in each plot. As the stars get closer, the initially spherical contours deform until merging, as illustrated by a cusp on the topmost figure. Afterwards, J^0 exhibits essentially quadrupolar-type oscillations.

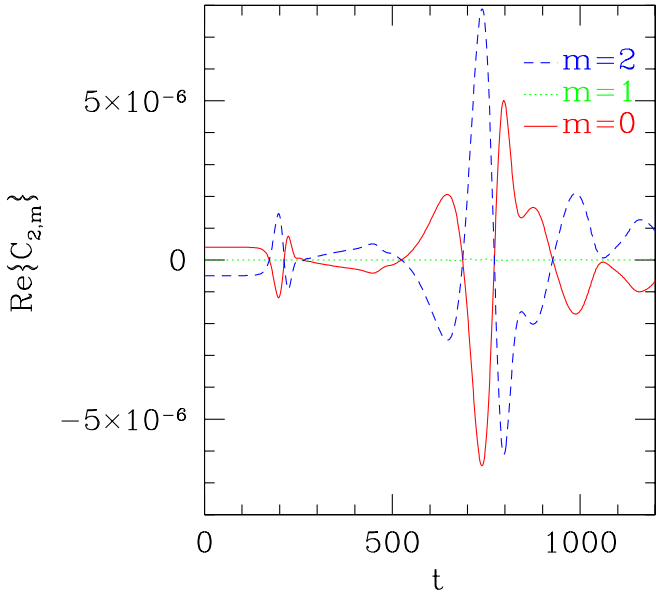

FIG. 10 (color online). *Boson/boson pair.* Coefficients corresponding to the $l = 2$ modes of $r\Psi_4$ as a function of time, extracted at $r_{\rm ext} = 200$. After some initial transient due to spurious radiation in the initial data, the signal is clearly visible corresponding to the merger of the stars and later decaying to smaller values. At late times, $t > 800$, contamination with boundary effects obscures the extracted signals.

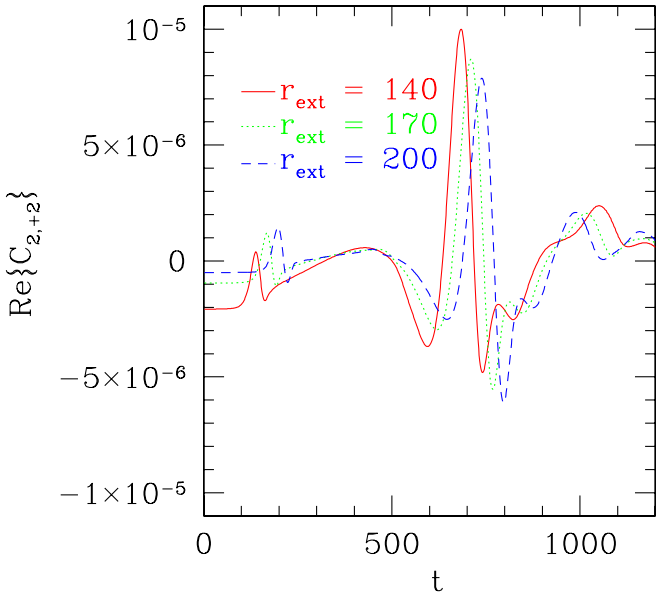

FIG. 11 (color online). *Boson/boson pair.* The coefficient $C_{2,+2}$ for different extraction radii. This figure illustrates both the outgoing waves due to the dynamics of the spacetime and the incoming waves that have traveled to the boundary and bounced off it. Additionally, some remnant dependence on r is visible indicating that the extraction is still performed not sufficiently far from the sources. Nevertheless, the structure of the outgoing waves is clearly visible.

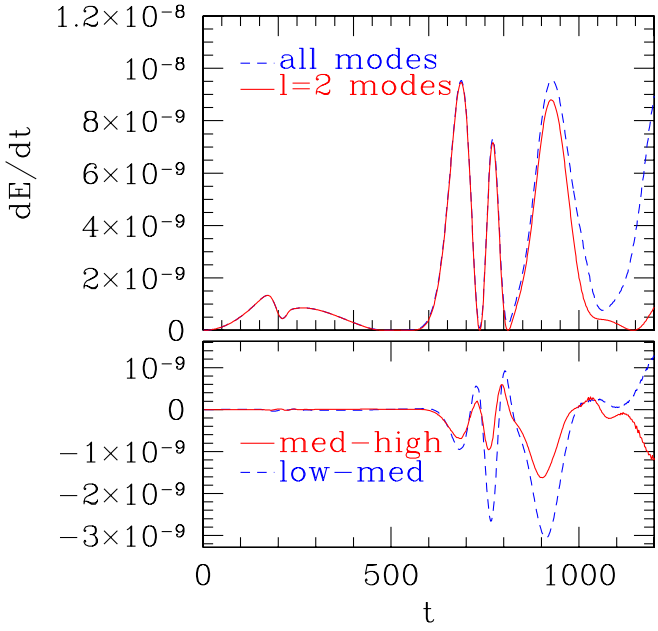

FIG. 12 (color online). *Boson/boson pair.* Radiated energy as a function of time. The top plot indicates the energy radiated in all modes (dashed line) together with that radiated solely in $l = 2$ modes. Clearly, until boundary effects begin to affect the results, practically all energy is radiated in the $l = 2$ modes. The bottom plot displays the difference between the $l = 2$ radiated energies at three different resolutions, indicating convergent behavior until $t \simeq 950$.

$$\phi^{(2)} = \phi_0(r)e^{-i(\omega t+\theta)} \tag{38}$$

with θ the relative phase. We will concentrate here on the extreme case, $\theta = \pi$, and so the stars are in phase opposition. Recall that, while Einstein equations are not sensitive to this phase difference, the Klein-Gordon equations are. Notice that in our head-on configuration the surface $x = 0$ is an antisymmetry plane for the scalar field, so it must remain zero in that plane. This symmetry may suggest that the boson stars will not merge, and this is precisely what is observed. As shown in Figs. 13 and 14, the behavior resembles what one would expect for two objects subject to a repulsive force but confined within a potential well. Such a scenario is supported by the analysis of Appendix B. Thus the objects oscillate about the coordinate position ($x = \pm 15$, $y = 0$, $z = 0$). Elucidating the final fate of this system will require much longer evolutions (making sure there is no causal interaction with the boundaries). Additional discussion, in light of results obtained from the other cases, can be found in the conclusion.

The gravitational radiation produced in this scenario is considerably weaker than the previous case, as the involved objects never acquire significant velocities to induce a strong time dependent quadrupole. In fact, our extracted radiation is of the same order as the spurious signal produced by the initial data. From these results

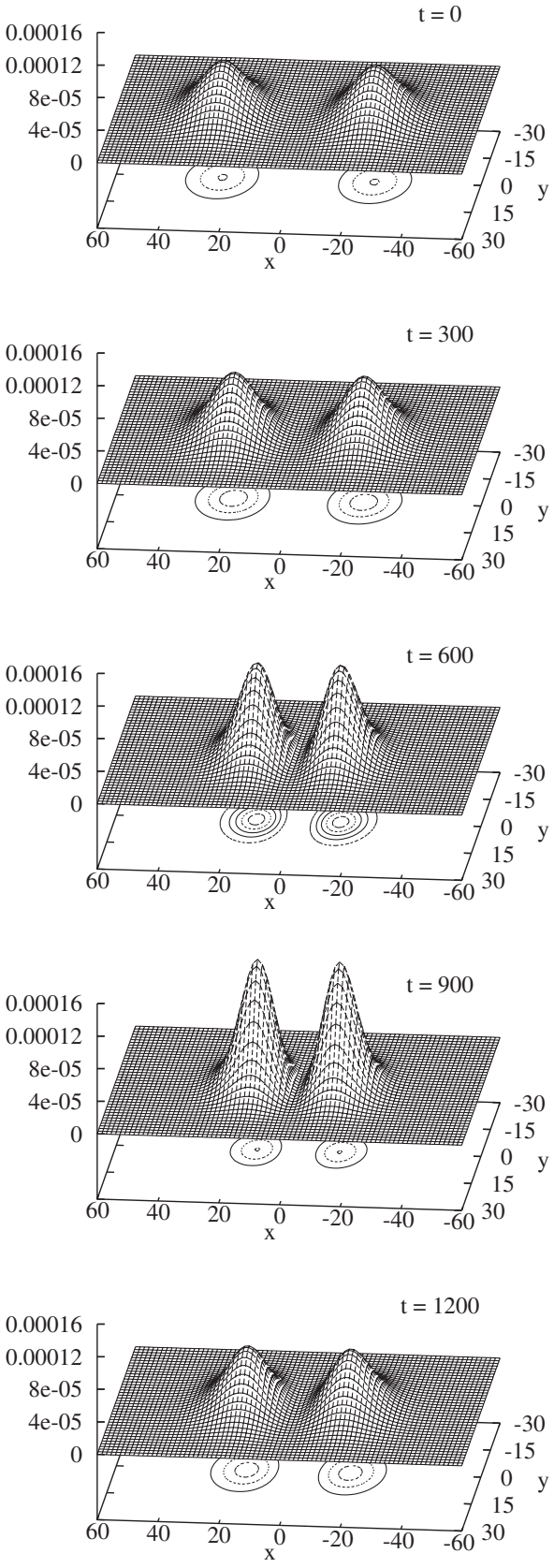

FIG. 13. *Boson/boson in opposition of phase pair.* 2D $z = 0$ cuts of the Noether density J^0 at different times Although the stars come closer, they never seem to merge.

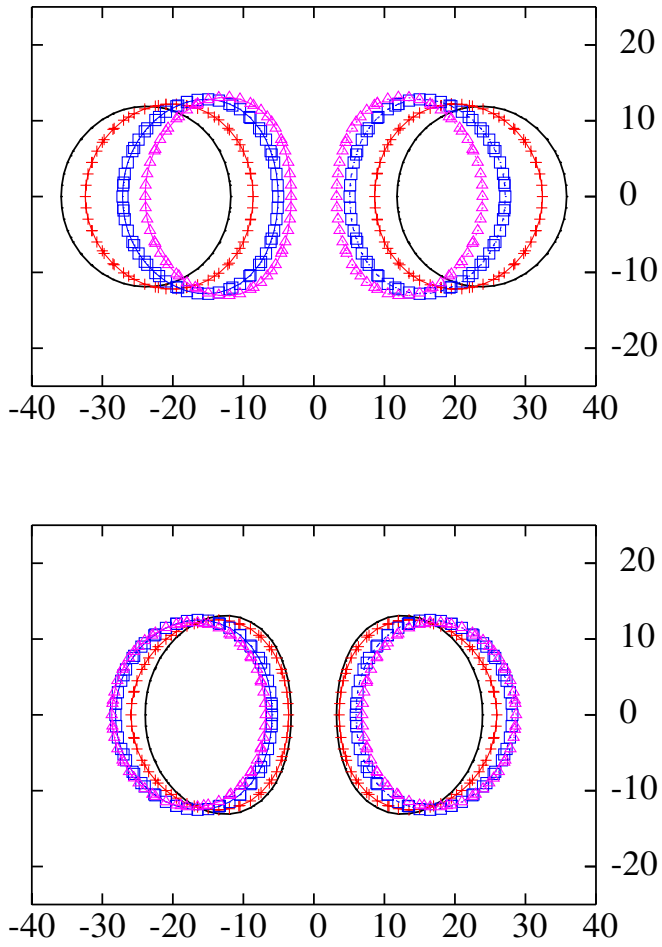

FIG. 14 (color online). *Boson/boson in opposition of phase pair.* Contours with value $J^0 = 2 \times 10^{-5}$ on the $z = 0$ plane. From top to bottom the contours are shown for times $\{180, 360, 540, 720\}$ and $\{720, 900, 1080, 1200\}$ indicated by solid lines, solid lines with crosses, solid lines with squares, and solid lines with triangles, respectively, in each plot. The stars initially get closer (top frame) but afterwards they move apart from each other (bottom frame); this process continues on as the stars are trapped in a common gravitational well.

coupled with the analysis presented in Appendix B, we conjecture that the maximum of the radiation happens at $\theta = 0$ while the minimum corresponds to $\theta = \pi$, just by assuming that the radiation is a smooth function of the phase difference. However, this must be substantiated by studying several representative cases.

3. Boson against antiboson

Another interesting case is the collision of a boson star with an otherwise identical star except with the opposite charge density. Such a star is called an antiboson star and rotates in the opposite direction as its partner in the complex plane. Recall that the initial value problem solution was degenerate upon the reflection $\omega \rightarrow -\omega$. Additionally, while this change leaves the geometry unchanged,

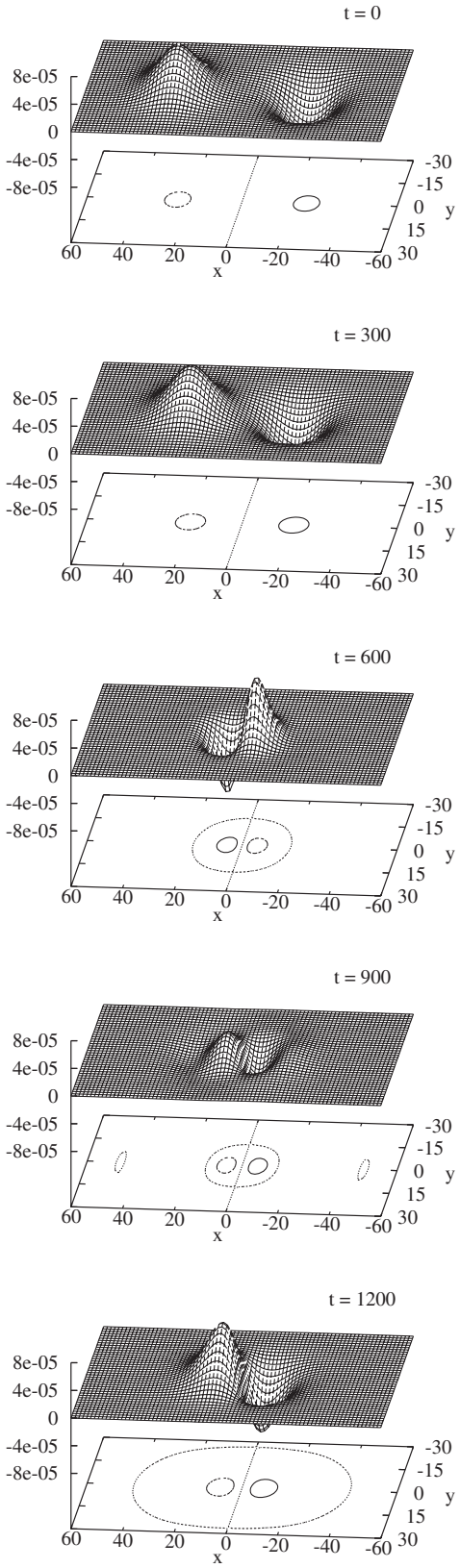

FIG. 15. *Boson/antiboson pair.* 2D $z = 0$ cuts of the Noether density J^0 at different times. Although the stars come closer and merge, the bosonic part is distinguishable from the antibosonic one by means of the different sign of the Noether density.

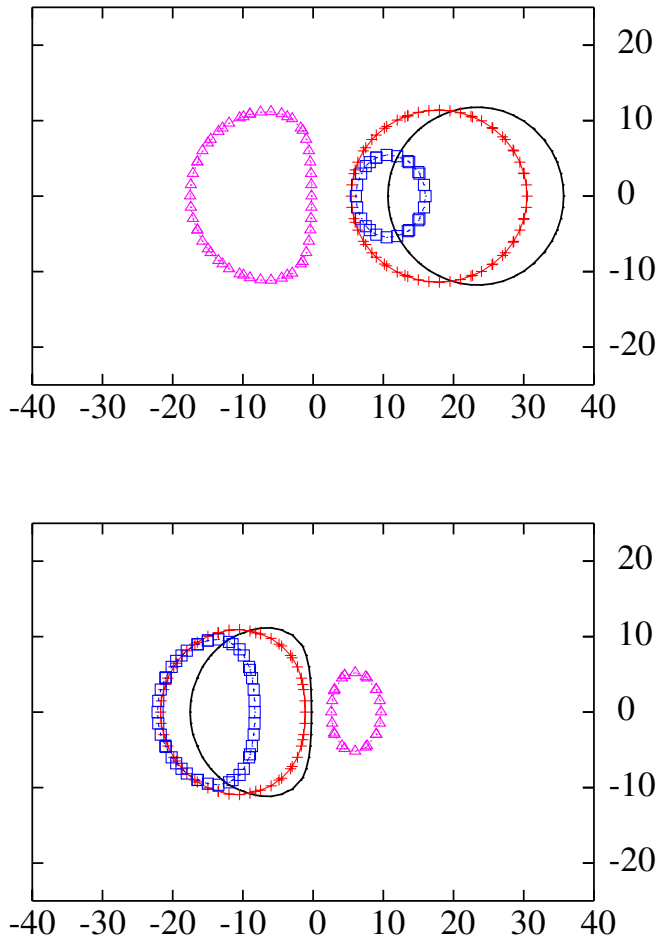

FIG. 16 (color online). *Boson/antiboson pair.* Contours with value $J^0 = 2 \times 10^{-5}$ on the $z = 0$ plane. From top to bottom contours are shown for times $\{180, 360, 540, 600, 660\}$ and $\{660, 780, 840, 900\}$ indicated by solid lines, solid lines with crosses, solid lines with squares, and solid lines with triangles, respectively, in each plot. Only the right star has such a contour initially as the left has a negative initial value for J^0. As the stars come closer to each other, the ''tunneling'' behavior is illustrated by the positive value appearing on the left side (top frame). As time progresses, this process essentially reiterates itself from the left side to the right side (bottom frame). The dynamics that follows repeats this side-to-side ''motion'' in the Noether density with the stars trapped in a common gravitational well.

the associated Noether change is affected by an overall sign change. In this section, we study the dynamical behavior of a binary system composed of a boson and an antiboson star. The initial conditions for such a scenario are simply obtained with the following choice,

$$\phi^{(1)} = \phi_0(r)e^{-i\omega t}, \tag{39}$$

$$\phi^{(2)} = \phi_0(r)e^{+i\omega t}. \tag{40}$$

We obtain the evolution of such a system, and as with the phase-opposition case, the early behavior agrees with that

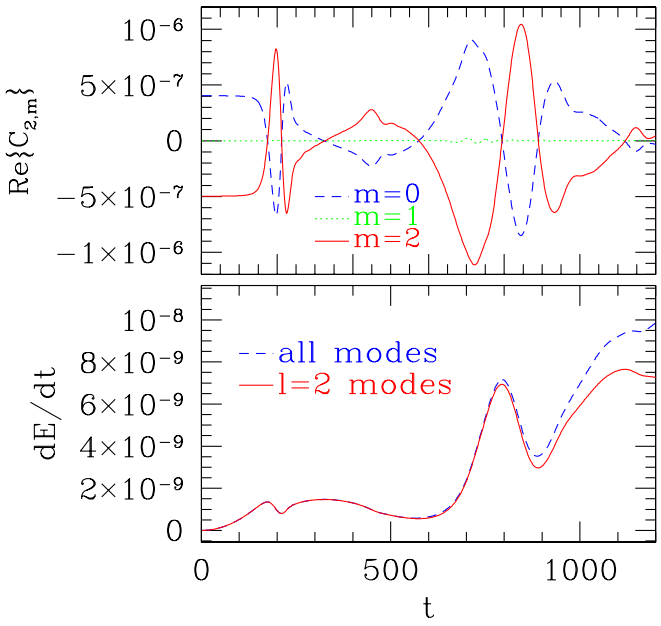

FIG. 17 (color online). *Boson/antiboson pair.* The $C_{2,m}$ coefficients of the $r\Psi_4$ decomposition (top frame) and the emitted radiation versus time (bottom frame).

of the boson-boson case. As time progresses, however, notable differences arise which are illustrated in Figs. 15 and 16. The dynamical behavior when the stars are close is less strong than in the boson-boson case but more so than in the boson-phase-opposition case. As a result, there is nontrivial generation of gravitational waves, though their time scale is longer than and their strength smaller than the boson-boson case. The total radiated energy, however, is similar as illustrated in Fig. 17.

V. CONCLUSIONS

We have studied the behavior of boson stars both in isolation and in head-on collisions with a three-dimensional implementation of the Einstein equations. Studies of the isolated star in Sec. IVA provided a nontrivial test of the implementation and showed it capable of accurately extracting delicate features of the solution such as the oscillation frequency. Additionally, by considering a coordinate condition not adapted to the static spacetime under study, the solution obtained further illustrated the ability of the harmonic coordinates to deal with compact objects in a smooth manner.

We then considered head-on collisions of different configurations of boson stars. Our studies revealed the interesting and varied phenomenology to which interacting boson stars can give rise. In particular, we have studied head-on configurations of equal-mass boson stars where their only differences could come from a reflection of their natural frequency or an overall phase difference. While their associated stress-energy tensor is insensitive to those options, the interaction gives rise to very different phenomenology. In fact, as is further supported by the discussion in Appendix B, this interaction is responsible for possible merger processes ranging from a simple-direct merger to a "repulsive-type" behavior while being trapped within a gravitational well.

The differences are further illustrated by taking a closer look at the position of the boson stars as well as the maximum of the energy density as a function of time. The positions are determined by the location where the energy density reaches a maximum in a given neighborhood. Figure 18 shows the proper distance between the origin and these maximums (i.e., that can be identified with the center of the boson stars) located in the $+x$ direction. Because of the symmetry of the problem, this is enough to draw conclusions on both stars. Included in the figure is the position a star would have as dictated by a simple Newtonian behavior of two-point particles with the mass of the boson star.

Notice that *a priori*, since the initial separation of the stars is of the same order of their radii, scalar-field interaction effects would be expected to become relevant early on. This is clearly visible for the boson-boson and boson-boson in phase-opposition cases; however, the Newtonian result is a reasonably good approximation for the boson-antiboson collision. This results from the significantly different interaction between their scalar fields in these cases, while in the boson-boson case a merger takes place

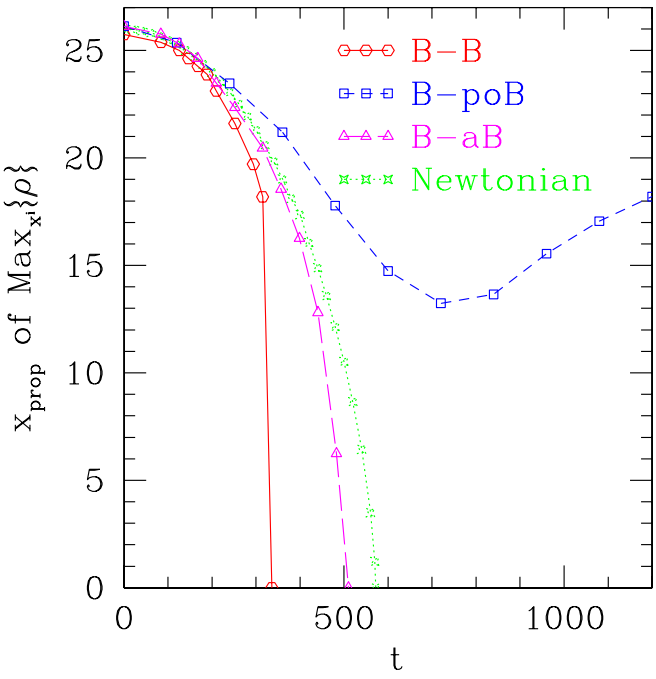

FIG. 18 (color online). The proper distance from the center of the boson star to the center of the computational domain as a function of time for the different cases and the Newtonian approximation. The position of the boson is identified with the maximum of the energy density.

at relatively early times, and in the boson-antiboson case the stars approach and essentially go through each other.

Additionally, this plot together with Fig. 19 (which shows the maximums of the energy density ρ) also explains, qualitatively, why the radiated energy is stronger for the boson-boson case since it is the one where the source's quadrupole has the most dynamic behavior. As a parenthetical remark, we note that the difference between the coordinate and the proper distances, during most of the evolution (the early part), is given in all cases by a slowly varying function of time, compared to the time scale of the solution. If the same behavior takes place in the binary black hole simulations presented, it would give further support to the comparison of the numerically calculated gravitational waves with those obtained from the quadrupole approximation based on the coordinate location of the black holes [42–45]. However, one must be cautious in the present case as we are considering a particular model to define the scalar fields through a single complex field.

Finally, it is also interesting to compare the observed behavior with those of similar scalar-field scenarios without gravitational interaction. This is the case of Q-balls [14] where boson-starlike configurations are obtained through the inclusion of a nontrivial potential in the Klein-Gordon equation. There one can also consider analogous situations, from the scalar-field point of view, such as those considered in this work. A qualitative comparison of the dynamics observed in both cases reveals that the inclusion of gravitational effects modifies the dynamics strongly. Besides not needing to boost the stars for a collision to take place, the gravitational attraction of the stars in our case is evidenced by the ''trapping'' of the stars instead of ''bouncing apart'' (for the boson-boson in phase opposition) or going through each other (for the boson-antiboson) as in [14]

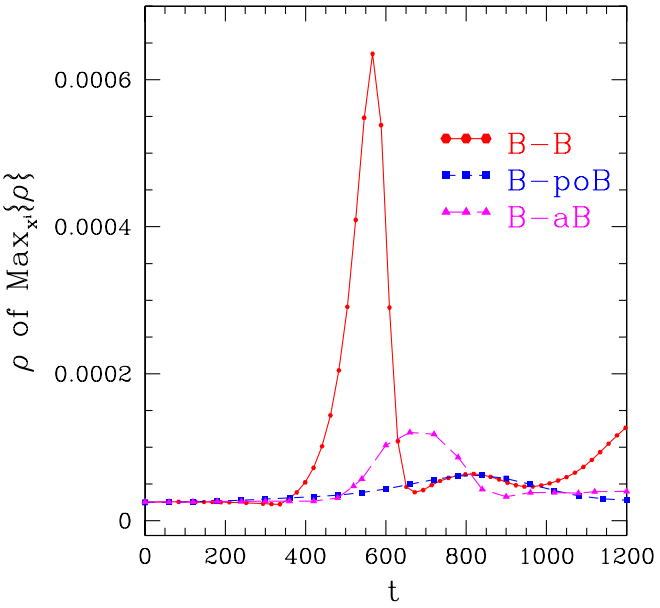

FIG. 19 (color online). The maximum of the energy density ρ is plotted as a function of time for the three different cases.

Summarizing, the results presented here illustrate the rich behavior displayed by binary boson-star dynamics even in the rather simple scenario of a head-on collision. In particular, the dependence on possible phase differences revealed that these phases strongly affect the outcome of the problem. In Appendix B is presented a simple treatment that sheds light on the influence that different phases between the stars or the frequency reflection in one of the them (boson/antiboson pair) can have on the dynamics of the problem. This treatment suggests that energy arguments explain why the boson-boson case gives rise to a merge while in the boson-opposition in phase boson case they seem to repel each other.

Additionally, these scenarios provided an excellent test of the implementation under strongly dynamical conditions. This implementation is being employed to deal with black hole spacetimes, and the results will be communicated elsewhere.

Having examined the landscape of head-on boson-star collision behavior, near future studies will concentrate on the more complex situations of orbiting cases as well as boson-star black hole binaries.

ACKNOWLEDGMENTS

We would like to thank M. Anderson, C. Bona, D. Garfinkle, E. Hirschmann, D. Nielsen, F. Pretorius, J. Pullin, and R. Wald for helpful discussions. This work was supported in part by NSF Grant No. PHY-0244699, No. PHY-0244335, No. PHY0326311, and No. PHY0554793 to Louisiana State University and No. PHY-0325224 to Long Island University. The simulations described here were performed on local clusters in the Department of Physics & Astronomy at LSU and the Department of Physics at LIU as well as on Teragrid resources provided by SDSC. L. L. is grateful to the Alfred P. Sloan Foundation and Research Corporation for financial support.

APPENDIX A: INITIAL DATA FOR AN ISOLATED BOSON STAR

The initial data for the boson-star configuration is computed first in spherical symmetry with a one-dimensional code. The resulting solution is then extended to three dimensions. The one-dimensional solution is obtained in the following way. First, we adopt a specific ansatz for the scalar field,

$$\phi(t, r) = \phi_o(r)e^{(-i\omega t)}. \tag{A1}$$

With this assumption, our goal is then to find $\phi_o(r)$, ω and the metric coefficients such that the spacetime generated by this matter configuration is static. We begin by considering the problem in polar-areal coordinates as is done, for

instance, in [2,8,9]. The line element in these coordinates takes the form

$$ds^2 = -\alpha(r)^2 dt^2 + a(r)^2 + r^2 d\Omega^2. \tag{A2}$$

The equilibrium equations in this coordinate system are then given by

$$a' = \frac{a}{2}\left\{-\frac{a^2-1}{r} + 4\pi r\left[\left(\frac{\omega^2}{\alpha^2} + m^2\right)a^2\phi_o^2 + \Phi_o^2\right]\right\}, \tag{A3}$$

$$\alpha' = \frac{\alpha}{2}\left\{\frac{a^2-1}{r} + 4\pi r\left[\left(\frac{\omega^2}{\alpha^2} - m^2\right)a^2\phi_o^2 + \Phi_o^2\right]\right\}, \tag{A4}$$

$$\phi_o' = \Phi_o, \tag{A5}$$

$$\Phi_o' = -(1 + a^2 - 4\pi r^2 a^2 m^2 \phi_o^2)\frac{\Phi_o}{r} - \left(\frac{\omega^2}{\alpha^2} - m^2\right)\phi_o a^2, \tag{A6}$$

where a prime denotes differentiation with respect to r. In order to obtain a solution of this system adapted to the desired physical situation, we provide the following boundary conditions:

$$a(0) = 1, \tag{A7}$$

$$\phi_o(0) = \phi_c, \tag{A8}$$

$$\Phi_o(0) = 0, \tag{A9}$$

$$\partial_r \alpha(0) = 0, \tag{A10}$$

$$\lim_{r\to\infty} a(r) = 1, \tag{A11}$$

$$\lim_{r\to\infty} \phi_o(r) = 0, \tag{A12}$$

$$\lim_{r\to\infty} \alpha(r) = 1, \tag{A13}$$

which guarantee regularity at the origin and asymptotic flatness. For a given value of ϕ_c, these equations and boundary conditions only admit solutions for a discrete set of values of ω. In our particular case, we are interested in the fundamental (lowest frequency) solution. The problem is solved by integrating from $r = 0$ outwards using a second order shooting method implemented with the numerical package LSODA [46]. The equations are integrated setting $\alpha(r = 0) = 1$ initially, and after all the equations are solved, the lapse is rescaled in order to obtain a function which asymptotes to 1 at infinity [47]. The same rescaling is then performed to the frequency ω.

Once the solution is computed in this coordinate system, a change of coordinates is performed to maximal isotropic ones:

$$ds^2 = \alpha^2(\tilde{r})dt^2 + \psi^4(\tilde{r})(d\tilde{r}^2 + \tilde{r}^2 d\Omega^2). \tag{A14}$$

In these coordinates the extension to three dimensions is direct since the space part of the metric is explicitly conformally flat. We perform the transformation of coordinates as in [8]. Since $\alpha(\tilde{r})$ and $\psi(\tilde{r})$ [and the scalar field $\phi_o(\tilde{r})$] are scalar functions of the spacelike hypersurface, and the time slicing is not changed, the extension to three dimensions involves only writing these functions as functions of x, y, and z such that $\tilde{r}^2 = x^2 + y^2 + z^2$. This task is performed using a five-point Lagrange interpolation.

This way we obtain initial data for g_{ab} and ϕ; the rest of the fields for the three-dimensional code are chosen as follows: $Q_{ab} = 0$, Π is computed from ansatz (A1), and D_{iab} and Φ_i are calculated using constraint equations (14). That completely defines the initial data for a boson star.

APPENDIX B: ENERGY CONSIDERATIONS

To gain some physical insight into these results, we consider here how the energy density behaves for the three different cases studied. To simplify the discussion, we consider the energy density in flat spacetime, i.e. we assume a Minkowski metric. Under this assumption, the energy density for a complex scalar field ϕ can be written as

$$\rho = \tfrac{1}{2}[|\Pi|^2 + |\Phi|^2 + m^2|\phi|^2] \tag{B1}$$

where Π and Φ are the derivatives of ϕ defined as before in Eqs. (13) and (14). Now, we treat the scalar field as given by the superposition $\phi = \phi_1 + \phi_2$ with ϕ_1, ϕ_2 describing the different stars we study. The energy density associated with this superposition can be expressed as

$$\rho = \rho_1 + \rho_2 + \Delta \tag{B2}$$

where ρ_i is the energy density that corresponds to the field ϕ_i in isolation and Δ is the interaction potential which vanishes when the stars are well separated. The interaction potential can then be written as

$$\Delta = \tfrac{1}{2}[\bar{\Pi}_1\Pi_2 + \Pi_1\bar{\Pi}_2 + \bar{\Phi}_1\Phi_2 + \Phi_1\bar{\Phi}_2 + m^2(\bar{\phi}_1\phi_2 + \phi_1\bar{\phi}_2)]. \tag{B3}$$

We next assume the scalar field has the form

$$\phi_1 = \phi_1^0(t, x^i)e^{i\omega t}, \tag{B4}$$

$$\phi_2 = \phi_2^0(t, x^i)e^{i(\epsilon\omega t+\theta)}, \qquad \epsilon = \pm 1 \tag{B5}$$

where ϕ_1 represents the complex field configuration associated with a dynamic boson star and ϕ_2 represents the field configuration of the other star. Both stars are characterized by the same frequency ω but the second star can be a regular boson ($\epsilon = 1$, $\theta = 0$), a boson in opposition of phase ($\epsilon = 1$, $\theta = \pi$), or an antiboson ($\epsilon = -1$, $\theta = 0$).

The profile of each is described by the real field $\phi_A^0(t, x^i)$ which is assumed to be a slowly varying function of time, so the most dynamical part of the time dependence is represented by the harmonic factor $e^{i\omega t}$.

Under these assumptions, a straightforward computation reveals that the effective interaction potential can be expressed as

$$\Delta = \Delta_0 \cos[(1 - \epsilon)\omega t - \theta]. \tag{B6}$$

Notice that when the two stars are centered in the same position the function Δ_0 is strictly non-negative, since it is a sum of quadratic terms,

$$\Delta_0 = [\bar{\Pi}_1^o \Pi_2^o + \Pi_1^o \bar{\Pi}_2^o + \bar{\Phi}_1^o \Phi_2^o + \Phi_1^o \bar{\Phi}_2^o + m^2(\bar{\phi}_1^o \phi_2^o + \phi_1^o \bar{\phi}_2^o)], \tag{B7}$$

and the behavior of the interaction term for each case considered is governed by that of $\cos[(1 - \epsilon)\omega t - \theta]$. Thus, for the problems analyzed in the present work, the interaction potential for each case is

$$\Delta_{\mathrm{B-B}} = \Delta_0, \qquad \Delta_{\mathrm{B-OPB}} = -\Delta_0, \qquad \Delta_{\mathrm{B-AB}} = \Delta_0 \cos(2\omega t). \tag{B8}$$

Since the contribution of Δ_0 is positive for the boson-boson case, the resulting gravitational potential associated with this case would be deeper than if not present. As a result, a merge of the two stars would seem a natural consequence. On the other hand, the Δ_0 contribution has the opposite sign for the boson-opposition phase boson case, translating into a gravitational potential exhibiting a bump at the center with two minimums around it. Such a bump would suggest that it is energetically preferable for the stars not to merge. Finally, the boson-antiboson interaction potential is governed by a varying function of time. If the interaction time scale is much longer than $\simeq 1/\omega$, the interaction term essentially integrates away to 0. Whether this is the case depends on the collision under study and, in particular, the stars' momentum as they come close to each other.

[1] J. A. Wheeler, Phys. Rev. **97**, 511 (1955).
[2] D. J. Kaup, Phys. Rev. **172**, 1331 (1968).
[3] R. Ruffini and S. Bonazzola, Phys. Rev. **187**, 1767 (1969).
[4] P. Jetzer, Phys. Rep. **220**, 163 (1992).
[5] E. W. Mielke and F. E. Schunck, Classical Quantum Gravity **20**, R301 (2003).
[6] E. W. Mielke, B. Fuchs, and F. E. Schunck, astro-ph/0608526.
[7] F. S. Guzman, Phys. Rev. D **73**, 021501(R) (2006).
[8] K. W. Lai, Ph.D. thesis, University of British Columbia, 2004.
[9] S. H. Hawley and M. W. Choptuik, Phys. Rev. D **62**, 104024 (2000).
[10] F. S. Guzman, Phys. Rev. D **70**, 044033 (2004).
[11] J. Balakrishna, R. Bondarescu, G. Daues, F. S. Guzman, and E. Seidel (unpublished).
[12] J. Balakrishna, Ph.D. thesis, Washington University, 1999.
[13] F. Pretorius (unpublished).
[14] R. A. Battye and P. M. Sutcliffe, Nucl. Phys. **590**, 329 (2000).
[15] A. Das, J. Math. Phys. (N.Y.) **4**, 45 (1963).
[16] Y. Choquet-Bruhat, Acta Math. **88**, 141 (1952).
[17] H. Friedrich, Commun. Math. Phys. **100**, 525 (1985).
[18] D. Garfinkle, Phys. Rev. D **65**, 044029 (2002).
[19] L. Lindblom *et al.*, Classical Quantum Gravity **23**, S447 (2006).
[20] Notice the factor of 2 difference between the formulation presented here and [19]. This is for convenience, as unnecessary factors of 2 are hence removed.
[21] C. Gundlach, G. Calabrese, I. Hinder, and J. M. Martin-Garcia, Classical Quantum Gravity **22**, 3767 (2005).
[22] M. Colpi, S. L. Shapiro, and I. Wasserman, Phys. Rev. Lett. **57**, 2485 (1986).
[23] P. Olsson, Math. Comput. **64**, 1035 (1995); **64**, S23 (1995); **64**, 1473 (1995).
[24] B. Gustafsson, H. Kreiss, and J. Oliger, *Time Dependent Problems and Difference Methods* (John Wiley and Sons, New York, 1995).
[25] D. Levy and E. Tadmor, SIAM J. Numer. Anal. **40**, 40 (1998).
[26] B. Strand, J. Comput. Phys. **110**, 47 (1994).
[27] G. Calabrese, L. Lehner, D. Neilsen, J. Pullin, O. Reula, O. Sarbach, and M. Tiglio, Classical Quantum Gravity **20**, L245 (2003).
[28] G. Calabrese, L. Lehner, O. Reula, O. Sarbach, and M. Tiglio, Classical Quantum Gravity **21**, 5735 (2004).
[29] L. Lehner, D. Neilsen, O. Reula, and M. Tiglio, Classical Quantum Gravity **21**, 5819 (2004).
[30] L. Lehner and O. Moreschi (unpublished).
[31] T. Baumgarte, P. Brady, J. Creighton, L. Lehner, F. Pretorius, and R. DeVoe (unpublished).
[32] M. Anderson, L. Lehner, I. Olabarrieta, C. Palenzuela, and S. L. Liebling (unpublished).
[33] M. J. Berger and J. Oliger, J. Comput. Phys. **53**, 484 (1984).
[34] S. L. Liebling, Phys. Rev. D **71**, 044019 (2005).
[35] S. L. Liebling, Classical Quantum Gravity **21**, 3995 (2004).
[36] L. Lehner, S. L. Liebling, and O. Reula, Classical Quantum Gravity **23**, S421 (2006).
[37] F. Pretorius, "Numerical simulations of gravitational collapse," The University of British Columbia, 2002.
[38] M. Anderson, E. Hirschmann, S. L. Liebling, and D. Neilsen, Classical Quantum Gravity **23**, 6503 (2006).
[39] D. Choi, K. W. Lai, M. Choptuik, E. Hirschmann, S. Liebling, and F. Pretorius (unpublished).

[40] T. Damour, in *300 Years of Gravitation*, edited by S. W. Hawking and W. Israel (Cambridge University Press, Cambridge, 1987), pp. 128–198.
[41] C. M. Will, Living Rev. Relativity **9**, 3 (2006), http://www.livingreviews.org/lrr-2006-3.
[42] A. Buonanno, G. B. Cook, and F. Pretorius, gr-qc/0610122.
[43] M. Campanelli, C. O. Lousto, and Y. Zlochower, Phys. Rev. D **73**, 061501 (2006).
[44] J. G. Baker, J. Centrella, D. I. Choi, M. Koppitz, and J. van Meter, Phys. Rev. D **73**, 104002 (2006).
[45] B. Bruegmann, J. A. Gonzalez, M. Hannam, S. Husa, U. Sperhake, and W. Tichy, gr-qc/0610128.
[46] L. R. Petzold and A. C. Hindmarsh, "LSODA," Computing and Mathematics Research Division, I-316 Lawrence Livermore National Laboratory, Livermore, CA 94550.
[47] This can be done because of the linearity of the slicing equation (A4).